# Supporting Information

## Keiluweit et al. 10.1073/pnas.1508945112

### SI Materials and Methods

**Litter Decomposition Study.** This study took advantage of an ongoing litter decomposition experiment at the H. J. Andrews Experimental Forest, Oregon, United States. About 90% of the area's annual precipitation falls from October to April, with the wettest period in December and peak drought conditions occurring in July. Within the HJA, the study was conducted at a site in watershed no. 8, at an elevation of 982 m and slope aspect of 223 degrees. Mean annual temperature at the nearby headquarters averaged 8.8 °C, and annual precipitation was 2,200 mm during 1974–2003 (46).

A rolling litter decomposition study spanning the years 2005–2011 was conducted at this site to examine the temporal and spatial variation in litter decomposition across individual layers. Nylon mesh panels (1-mm netting, 60 × 60-cm frames) were placed on the litter surface at this site annually. They were stacked over time to delineate annual litter fall from that of the subsequent year without restricting process intensities by artificial closure. Upon harvest at the end of the dry season in November 2011, the whole littercake was transferred on a supporting sheet and placed in a sealed plastic container. Recent needles and underlying O, A, and B horizon material were also collected and placed in amber vials and zip lock bags. Samples were transported at 4 °C and immediately returned to the laboratory. In the laboratory, individual layers of the littercake were separated, and decaying needles were manually separated from other forms of litter, such as cones and twigs. Soils were pushed through a 2-mm sieve and mixed thoroughly. Needle litter from each individual layer and the underlying soil horizons were then subsampled for laboratory analyses. Any variability reported included effects of subsampling and laboratory procedures. One subsample from each litter layer and mineral soil horizon was processed at field moisture for wet-chemical extractions and microscopic analyses. For spectroscopic analyses, another subsample was dried in an anaerobic glove box at room temperature in the dark to prevent changes in Mn oxidation state. A third subsample was oven-dried (50 °C, overnight) and ground for litter chemistry analyses.

**Manganese Chemistry.** Total Mn (as well as Fe, Ca, and Al) content was quantified with X-ray fluorescence spectrometry (XEPOS HE XRF spectrometer; SPECTRO Analytical Instruments). To determine the amount of bioavailable Mn, we additionally quantified soluble and organically complexed Mn ($Mn_{pyro}$) using an Na-pyrophosphate extraction (49). Briefly, an aliquot of field-moist needle litter or soil equivalent to 200 mg of oven-dry sample was combined with 14 mL of 0.1 M Na-pyrophosphate solution at pH 10 in a 15-mL polypropylene centrifuge tube, agitated in the dark using a reciprocal shaker for 8 h, and centrifuged at 17,000 × *g* for 15 min. After centrifugation, the supernatant was removed, filtered through 0.22-μm syringe filters, and stabilized in 1% high-purity $HNO_3$. Concentrations of Mn (as well as Fe, Ca, and Al) in the extract were determined on a Perkin-Elmer SCIEX Elan DRC II inductively coupled plasma mass spectrometer (ICP-MS).

Mn oxidation state was determined using Mn XANES. Anaerobically dried litter and soil samples were hand-ground in the glove box, densely packed in poly(tetrafluoroethylene) sample holders, and sealed with X-ray transparent Kapton tape. Mn XANES spectra were recorded at the wiggler beamline 4-3 at the Stanford Synchrotron Radiation Lightsource (SSRL) with an Si(110) $\phi = 0$ double-crystal monochromator, and fluorescence yield was collected with a Stern–Heard ion chamber detector (51). Background subtraction, normalization, and fitting of the spline function were performed on the collected spectra using the Athena software package (52). The average oxidation state of Mn was derived from individual spectra using a linear-combination fitting procedure (50). The procedure uses 17 pure valence $Mn^{2+}$, $Mn^{3+}$, and $Mn^{4+}$ reference standards available (open-source, web link available in ref. 48), and fitting results are summarized in Table S3. In Manceau et al. (50), this method yielded the correct average valences to within about 0.04 valence units, and the correct fractions of the $Mn^{2+}$, $Mn^{3+}$, and $Mn^{4+}$ states to within 4.4–4.6% when applied to the collection of mixed-valence Mn minerals. Based on the deviation between the sum of the three fractions from unity (Table S3), we estimate the error in our study to be <8% for bulk XANES and <11% for μXANES.

**Litter Decomposition State.** Total C and N contents were determined using a Europa Scientific 20/20 isotope ratio mass spectrometer. Changes in the organic composition of the decomposing litter were determined using FTIR spectroscopy. FTIR spectra of the samples pressed in KBr pellets were recorded from 4,000 to 650 $cm^{-1}$ with a resolution of 4 $cm^{-1}$ on a Thermo Nicolet NEXUS 670 FTIR spectrometer (Thermo Fisher Scientific). For each sample, 512 scans were collected in transmission mode and averaged before Fourier transform processing. Three pellets were prepared and analyzed for each sample, and the resulting spectra were averaged. The OMNIC software package (Thermo Fisher Scientific) was used on the fingerprint region of the spectra (1,800–850 $cm^{-1}$) to perform baseline correction, normalization, and peak deconvolution on the spectra.

$^{13}$C-NMR experiments were performed on a Bruker Avance 400 spectrometer at 100 MHz (400 MHz $^{1}$H frequency). All experiments were performed with 4-mm sample rotors in a double-resonance probe head. Semiquantitative structural information on all carbons in the sample was obtained by $^{13}$C cross polarization/total sideband suppression (CP/TOSS) as described in ref. 28. The NMR experiments were conducted at a spinning speed of 5 kHz and a CP time of 1 ms, with a $^{1}$H 90° pulse length of 4 μs and a recycle delay of 1 s. Four-pulse total suppression of sidebands was used before detection, and two-pulse phase-modulated decoupling was applied for optimum resolution. The corresponding subspectrum, with signals of nonprotonated carbons and carbons of mobile groups such as rotating $CH_3$, was obtained by $^{13}$C CP/TOSS combined with 40-ms dipolar dephasing (DD). The spectra and subspectra obtained with CP/TOSS and CP/TOSS with DD were assigned to different carbon functional groups following previous literature (53–56).

To identify molecular changes in aromatic components of the litter (lignins and tannins), synchrotron-based laser desorption post ionization (LDPI) mass spectrometry of fresh needles and litter layers was performed on a modified time-of-flight secondary ion mass spectrometer (TOF.SIMS V; IonTOF) coupled to a synchrotron UV light port at beamline 9.0.2 of the Advanced Light Source, Lawrence Berkeley National Laboratory (29, 31). Before analysis, 3 mg of ground needle material was suspended in high-purity (99.9%) MeOH, pipetted on silicon substrates (Wafer World), and dried in a clean hood under constant $N_2$ gas flow. The desorption laser was calibrated to emit 8.5-ns pulses focused to a spot diameter of ∼30 μm, and its power was reduced until no laser-induced fragmentation could be detected in the background (∼0.7 $MW \cdot cm^{-2}$) while achieving sufficient desorption efficiency. Under ultra-high vacuum, the sample was scanned with the laser with 2 $mm \cdot s^{-1}$ over a 20-mm distance to avoid

sample damage. To optimize the signal-to-noise ratio (S/N), mass spectra collected during each scan were the sum of ~16,000 laser shots on the surface. We performed three replicate scans for each sample, and mass spectra are presented as averages normalized to the total intensity.

Zimmermann and coworkers (29, 30) showed that aromatic ring structures with *m/z* ratios greater than 100 have significantly lower IE (<8.5 eV) than other environmentally relevant compound classes (>9 for alcohols, alkanes, and alkenes). Using synchrotron-LDPI, we exploited this fact for selective detection of aromatic analytes within the mixture of organic compounds found in litter. To confirm that the most prominent mass peaks (e.g., $m/z$ = 340, 370, 396, 399, 400, 406, and 414) in our mass spectra correspond to aromatic structures, we determined ionization energies (IEs) for each of the mass peaks in a second LDPI experiment as previously described (31, 32). Briefly, IEs were determined by varying the incident UV photon energy (i.e., the ionization energy) between 7.5 and 12.5 eV in 1-eV increments, and we then collected the resulting mass spectra. Normalized relative intensity of the mass peak of interest was then plotted against the photon energy used for each scan (Fig. S2). Using a linear fit, the intercept with the ordinate (photon energy) represents the IE of a given mass peak (listed in Table S2). Peaks at *m/z* ratios of 340, 368, 396, 399, 400, 406, and 412 showed IEs of ≤8.5 eV and were thus attributed to aromatic moieties.

**Chemical Imaging Analyses.** Needles from all layers were visibly colonized by fungal hyphae, frequently concentrated around dark infections of the surface. To determine Mn distribution and oxidation state associated with these fungal infections, elemental maps and Mn XANES spectra of cross-sectioned needle litter were obtained using X-ray fluorescence mapping and X-ray absorption spectroscopy (μXRF/XAS). To this end, individual needles taken from the top layer were embedded in epoxy (Spurr; TedPella) and cured. Cross-sections were obtained by cutting the resin block and polishing the exposed surface using sand paper and diamond paste. μXRF maps and μXANES spectra were collected at the hard X-ray microprobe beamline 10.3.2 at the Advanced Light Source (ALS) at Lawrence Berkeley National Laboratory. μXRF maps were acquired by continuously raster scanning the sample with a 5 × 5-μm beam in 5-μm steps and a 100-ms count time. Maps were collected with the incident photon energy set at 7,000 and 10,000 eV, and the fluorescent peaks for K, Ca, Ti, Si, Cr, Mn, Fe, Ni, Cu, and Zn were obtained at each energy. The fluorescence yield was normalized by $I_0$ and the dwell time. Several regions of interest were selected from the μXRF maps for Mn K-edge μXANES analysis. Fluorescence yield was recorded in QuickXANES mode (30 single spectra) to acquire data with minimal beam damage per spot. QuickXANES spectra were checked for beam damage, and, if necessary, spectra showing evidence for beam reduction were excluded from further analysis. In all cases, a minimum of five QuickXANES spectra were averaged for each region of interest, and the resulting spectra were calibrated and normalized as described for bulk Mn XANES spectra.

To obtain high-resolution maps of the functional group chemistry at the hyphae–needle interface, thin sections of infected needles from the top layer were also prepared using a cryostat (Leica 1950 Cyrostat; Leica Instruments) without the use of carbon-based resins. Before sectioning, needles were surrounded by MilliQ $H_2O$ and flash frozen in liquid $N_2$. The specimens were then removed from the tube and transferred on a chuck mount that was allowed to equilibrate to cutting temperature in the cryostat for 30 min. To attain 5-μm sections, the cryostat was set to −18 °C chamber temperature and −16 °C mount temperature. A 70-μm curl guard was adjusted as needed to achieve flat, nondeformed sections. Flat sections were transferred to gold-coated (IR reflective) microscope slides, and needle surfaces infected with fungi were identified using a light microscope. High-resolution infrared maps of these locations were acquired using synchrotron FTIR (SR-FTIR) spectromicroscopy at ALS beamline 1.4.3 (Lawrence Berkeley National Laboratory). Maps were collected on a Nicolet Nic-Plan IR microscope (Thermo Fisher Scientific) equipped with a liquid-$N_2$ cooled mercury-cadmium telluride (MCT) detector connected to the synchrotron light source. All maps were collected by point-by-point raster scanning of the thin sections using a 32× Reflachromat Nicolet objective with a 2-μm spot size. For each spot, 64 scans were collected from 4,000 to 650 $cm^{-1}$ at a resolution of 4 $cm^{-1}$. After completion of the SR-FTIR analysis, μXRF maps of the same regions were collected with a 3 × 3-μm beam in 2-μm steps and a count time of 100 ms. μXANES spectra at the Mn K-edge of regions of interest identified in the μXRF maps were acquired as outlined above.

**Data Analysis.** All statistical analyses were performed using OriginPro (OriginLab). Reported SEs are based on three analytical replicates.

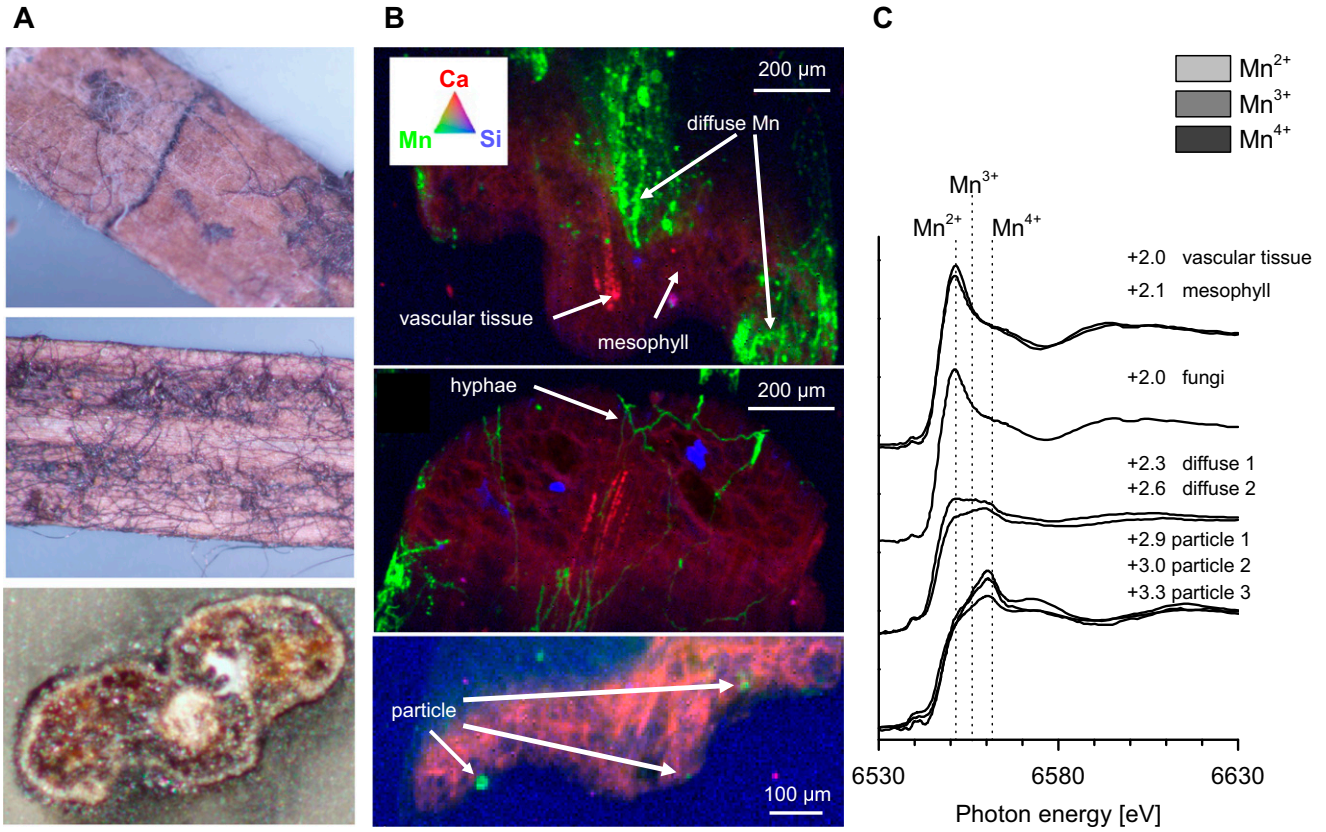


**Fig. S1.** µ-XRF/XAS analysis of whole needle cross-sections taken from the top litter layer (year 1). (*A*) Photographs showing individual needles colonized by fungal hyphae associated with dark patches. (*B*) False color XRF maps of resin-embedded needle cross-sections showing the concentration of Mn (green) dense patches, hyphae and particles in contrast to Ca (blue) and Si (red). Color intensity is directly related to elemental concentrations. The apparent 3D appearance of the map is due to the penetration of X-rays ~100–200 µm into the resin-embedded cross-sections. (*C*) Mn XANES spectra of the regions highlighted in *B*, illustrating the more oxidized state of Mn in diffuse patches and particles associated with the needle surfaces. Pie charts show the relative amounts of $Mn^{2+}$, $Mn^{3+}$, and $Mn^{4+}$ and the number denoting the average valence state as determined by linear combination fitting (50).

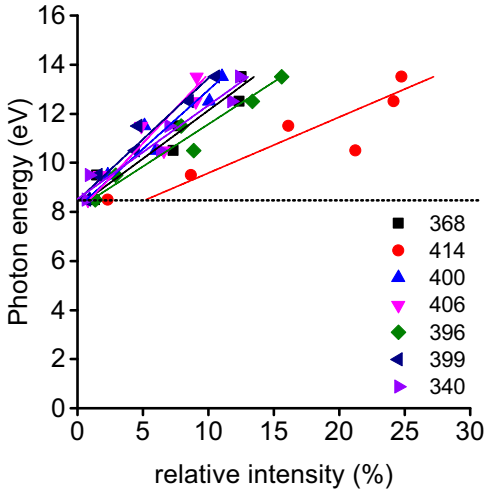


**Fig. S2.** Signal intensity of mass peaks (*m/z* ratios ranging from 340 to 414) plotted against incident photon energies (ranging from 8.5 to 13.5 eV with 1 eV increments). The ordinate intercept of the linear fit approximates the ionization energy (IE) for the respective mass fragment. Mass peaks with ionization energies ≤ 8.5 eV (dotted line) are identified as aromatic moieties. In this case, all fits intercept the ordinate at energies equal or below 8.5 eV.

**Table S1. Chemical transformations of litter over 6 y of decomposition**

| | | | | | | | FTIR[‡] relative absorbance, % | | | LDPI[§], relative intensity, % | | $^{13}$C-NMR[¶] | | | |
|---|---|---|---|---|---|---|---|---|---|---|---|---|---|---|---|
| | | | | | | | | | | | | Aromatic | | Sacch | Aliphatics |
| Sample | Year | C/N*, ratio | $Mn_{total}$*, mg·g$^{-1}$ | $Mn_{pyro}$*, % | $Mn_{red}$*, % | $Mn^{+x}$† | Amide | Aromatic | Sacch | $\sum ar^-$ | $\sum ar^+$ | $C_{ar}$-O | $C_{ar}$-R | C-OH | $CH_x$ |
| Fresh needles[#] | 2012 | 48 ± 2 | 0.9 ± 0.1 | 55 ± 1 | 45 ± 9 | 2.07 | 13 | 0.7 | 47 | n.a. | n.a. | n.a. | n.a. | n.a. | n.a. |
| Litter layer 1 | 2011–10 | 47 ± 2 | 1.2 ± 0.0 | 66 ± 3 | 34 ± 3 | 2.15 | 15 | 0.9 | 46 | 5 | 1.5 | 6.5 | 10.6 | 39 | 20 |
| Litter layer 2 | 2010–09 | 39 ± 3 | 1.5 ± 0.1 | 74 ± 4 | 26 ± 2 | 2.22 | 17 | 1.1 | 44 | 4 | 2.3 | 7.0 | 10.7 | 37 | 22 |
| Litter layer 3 | 2009–08 | 35 ± 1 | 1.8 ± 0.1 | 85 ± 4 | 15 ± 1 | 2.31 | 20 | 1.1 | 44 | 3 | 1.4 | 8.0 | 11.1 | 35 | 22 |
| Litter layer 4 | 2008–07 | 37 ± 2 | 2.1 ± 0.1 | 87 ± 6 | 14 ± 1 | 2.49 | 22 | 1.3 | 42 | 3 | 2.3 | 8.2 | 11.7 | 32 | 23 |
| Litter layer 5 | 2007–06 | 36 ± 1 | 2.5 ± 0.1 | 83 ± 4 | 17 ± 2 | 2.59 | 21 | 1.2 | 44 | 2 | 2.4 | 8.7 | 12.5 | 32 | 22 |
| Litter layer 6 | 2006–05 | 38 ± 1 | 2.5 ± 0.1 | 74 ± 3 | 26 ± 2 | 2.74 | 21 | 1.4 | 41 | 2 | 2.5 | 8.7 | 13.1 | 29 | 25 |
| O horizon (needle litter) | <2005 | 45 ± 2 | 1.4 ± 0.2 | 72 ± 2 | 28 ± 6 | 2.83 | n.a. | n.a. | n.a. | n.a. | n.a. | n.a. | n.a. | n.a. | n.a. |
| A horizon (2–20 cm) | n.a. | 24 ± 1 | 1.0 ± 0.1 | 26 ± 2 | 74 ± 11 | 3.14 | n.a. | n.a. | n.a. | n.a. | n.a. | n.a. | n.a. | n.a. | n.a. |
| A/B horizon (20–37 cm) | n.a. | 23 ± 2 | 0.9 ± 0.0 | 5 ± 0 | 95 ± 4 | 3.03 | n.a. | n.a. | n.a. | n.a. | n.a. | n.a. | n.a. | n.a. | n.a. |

Sacch, saccharides; n.a., not available.

*Values given as mean ± SE. SEs are based on three analytical replicates.

†x, average oxidation state of Mn as determined by linear combination fitting of Mn XANES spectra.

‡Peak deconvolution results for absorbance bands at 1,640–1,700 and 1,580–1,530 (amide I and II), 1,510 (lignin), and 1,180–950 (saccharides) cm$^{-1}$.

§$\sum ar^-$ and $\sum ar^+$ denote the sums of peak intensities of masses identified in LDPI spectra shown in Fig. 2*C*. $\sum ar^+$ is the sum of normalized intensities of peaks that increase with litter age ($m/z$ = 340–370) whereas $\sum ar^-$ represents the sum of normalized intensities of peaks decreasing over time ($m/z$ = 396–414).

¶Peak integration results using chemical shift regions of 0–47 (aliphatic), 92–58 (saccharides), and 140–112/160–140 ppm ($C_{ar}$-R/$C_{ar}$-O aromatic).

#Reported values are for mature needles on the tree (6 y and older). Young needles (younger than 1 y) showed significantly lower Mn contents (0.2 mg·g$^{-1}$).

**Table S2. Ionization energies for fragments associated with most prominent mass peaks and their evolution over 6 y of litter decomposition**

| *m/z* | 340 | 368 | 396 | 399 | 400 | 406 | 414 |
|---|---|---|---|---|---|---|---|
| Sum peak intensity | $\sum ar+$ | $\sum ar+$ | $\sum ar^-$ | $\sum ar^-$ | $\sum ar^-$ | $\sum ar^-$ | $\sum ar^-$ |
| Ionization energy | 8.5 | 8.2 | 8.1 | 8.5 | 8.2 | 8.0 | 7.3 |
| Correlation coefficient ($R^2$) | 0.94 | 0.82 | 0.94 | 0.96 | 0.92 | 0.86 | 0.92 |

$\sum ar^-$ and $\sum ar^+$ denote the sums of peak intensities of masses identified in LDPI spectra shown in Fig. 2*C*. $\sum ar^+$ is the sum of normalized intensities of peaks that increase with litter age (*m/z* = 340–368) whereas $\sum ar^-$ represents the sum of normalized intensities of peaks decreasing over time (*m/z* = 396–414).

**Table S3. Fractional and average valence states of Mn obtained from a linear combination fit of Mn XANES spectra as described in ref. 50**

| | | Relative contribution, % | | | | | |
|---|---|---|---|---|---|---|---|
| Figure | Location | $Mn^{2+}$ | $Mn^{3+}$ | $Mn^{4+}$ | Avg Mn valence | Sum | NSS × $10^{-3}$ |
| Fig. 1 | Fresh litter | 93 | 7 | 0 | 2.07 | 1.08 | 0.9 |
| | Layer 1 | 85 | 15 | 0 | 2.14 | 1.06 | 0.9 |
| | Layer 2 | 78 | 22 | 0 | 2.22 | 1.01 | 0.7 |
| | Layer 3 | 74 | 20 | 6 | 2.31 | 1.04 | 0.3 |
| | Layer 4 | 67 | 17 | 16 | 2.49 | 1.01 | 0.4 |
| | Layer 5 | 59 | 22 | 18 | 2.59 | 1.00 | 0.3 |
| | Layer 6 | 49 | 28 | 23 | 2.74 | 0.99 | 0.4 |
| | O horizon | 46 | 24 | 30 | 2.83 | 0.97 | 0.5 |
| | A horizon | 29 | 28 | 43 | 3.14 | 0.93 | 0.2 |
| | A/B horizon | 33 | 31 | 36 | 3.02 | 1.00 | 0.2 |
| Fig. S1 | Mesophyll | 99 | 0 | 1 | 2.02 | 0.95 | 0.2 |
| | Mesophyll | 88 | 12 | 0 | 2.12 | 0.98 | 0.3 |
| | Fungi | 99 | 0 | 1 | 2.02 | 0.99 | 0.2 |
| | Diffuse spot | 72 | 0 | 28 | 2.57 | 1.00 | 1.3 |
| | Diffuse spot | 83 | 4 | 13 | 2.30 | 0.96 | 0.9 |
| | Particle 1 | 45 | 21 | 35 | 2.90 | 1.11 | 2.4 |
| | Particle 1 | 49 | 0 | 51 | 3.01 | 1.05 | 0.5 |
| | Particle 1 | 27 | 20 | 53 | 3.26 | 1.01 | 0.2 |
| Fig. 4*D* | Spot 1 | 85 | 15 | 0 | 2.15 | 1.05 | 4.7 |
| | Spot 2 | 88 | 12 | 0 | 2.12 | 1.00 | 3.6 |
| | Spot 3 | 43 | 57 | 0 | 2.57 | 1.10 | 9.2 |
| | Spot 4 | 48 | 48 | 4 | 2.57 | 1.03 | 1.3 |
| | Spot 5 | 27 | 73 | 0 | 2.73 | 1.04 | 6.4 |

*NSS*, the normalized sum-squared residual = $\sum n(\text{data} - \text{fit})/\sum n(\text{data})$.